J. Fluid Mech. (2006), *vol.* 549, *pp.* 1–23. © 2006 Cambridge University Press
doi:10.1017/S0022112005007226 Printed in the United Kingdom

On the realm of validity of strongly nonlinear asymptotic approximations for internal waves

By R. CAMASSA[1], W. CHOI[2], H. MICHALLET[3],
P.-O. RUSÅS[4] AND J. K. SVEEN[5]

[1]Department of Mathematics, University of North Carolina, Chapel Hill, NC 27599, USA

[2]Department of Naval Architecture & Marine Engineering, University of Michigan,
Ann Arbor, MI 48108, USA

[3]Laboratoire des Ecoulements Géophysiques et Industriels, BP53, 38041 Grenoble Cedex 9, France

[4]Faculty of Computer Sciences, Østfold University College, Norway

[5]Mechanics Division, Department of Mathematics, University of Oslo, Norway

(Received 7 April 2004 and in revised form 8 July 2005)

Analytical and numerical results from recently developed strongly nonlinear asymptotic models are compared and validated with experimental observations of internal gravity waves and results from the numerical integrations of Euler equations for solitary waves at the interface of two-fluid systems. The focus of this investigation is on regimes where large amplitudes are attained, where the classical weakly nonlinear theories prove inadequate. Two asymptotically different regimes are examined in detail: shallow fluids, in which the typical wavelengths of the interface displacement are long with respect to the depths of both fluids, and deep fluids, where the wavelengths are comparable to, or less than, the depth of one of the two fluids. With the aim of illustrating the breakdown of the asymptotic assumptions, the transition from a shallow to a deep regime is examined through numerical computation of Euler system's solutions and by comparisons with solution to models.

1. Introduction

The problem of internal gravity wave dynamics in stratified fluids is experiencing increased attention, spurred on in part by improvements in detection technology and by heightened appreciation of the role played by these waves in environmental issues, e.g. in near-coastal dynamics. Recent observations show that large-amplitude internal waves frequently occur, see for instance Stanton & Ostrovsky (1998), Liu *et al.* (1998), Orr & Mignerey (2003), and Zeng & Alpers (2004). A collection of synthetic aperture radar (SAR) images in different ocean basins is available in Jackson (2004) and shows that large-amplitude internal waves are a common phenomenon in the oceans.

Mathematically, the large-amplitude regimes which are easily attained by internal waves, both experimentally and in the field, make this class of wave phenomena especially challenging. In particular, the strong nonlinearity causes the failure of models based on the quasi-linear approximation of the fundamental equations of motion. These equations, be they the Euler system, or the full Navier–Stokes equations when viscous effects must be included, are hardly amenable to analytic methods of solution and can be very costly to simulate in even relatively simple situations. Thus, there is a need for models that are sufficiently accurate to capture the dynamics

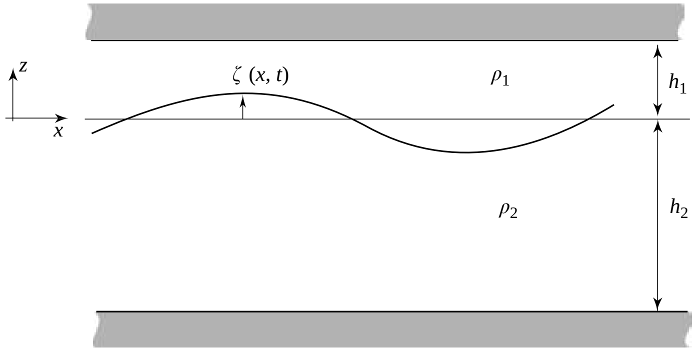

FIGURE 1. The two-fluid system set-up and relevant notation.

occurring in physically realistic situations, yet that are simple enough to be efficiently simulated numerically.

The simplest physical situation capable of supporting internal wave motion is that of a two-layer fluid under gravity, where the density is a different constant on each side of an interface, see figure 1. Though very crude, this set-up is routinely used as a building block for more refined descriptions, e.g. for approximating near constant density variations by piecewise constant steps (see, e.g. Baines 1995; Pedlosky 1979) and so this idealization deserves some attention. Even by restricting the upper (free) surface with a rigid lid, and considering the fluid as incompressible and inviscid, the added complexity of fluid motion with respect to that of a single homogeneous layer is substantial. At least two more parameters enter the problem, the density ratio and the ratio of undisturbed layer thicknesses. A variety of situations can be envisaged; however, for geophysical applications, the density ratio ρ_1/ρ_2 between the first (upper) layer and the second (lower) layer is always close to unity (with $\rho_1 < \rho_2$ for stability), and the ratio h_1/h_2 between (undisturbed) layer thicknesses plays the most important role. Thus, throughout this work we will consider the density ratio ρ_1/ρ_2 as fixed and independent of the other parameters.

Starting from the Euler system governing the motion of each fluid layer, the classical weakly nonlinear theories of long-wave motion assume that the typical amplitude a of the waves is small compared with both layer thicknesses, or $\alpha \equiv |a|/h_i \ll 1$, $i = 1, 2$, and distinguish between a shallow configuration, where the horizontal length scale λ of the motion is large with respect to both h_1 and h_2, i.e. $\epsilon \equiv h_i/\lambda \ll 1$, and a deep configuration, where λ is large with respect to just one layer, i.e. $h_i/\lambda \ll 1$, $i = 1$ or $i = 2$ (but not both). Based on the rate of steepening by nonlinearity and flattening by dispersion that the two parameters α and ϵ represent, a balance is postulated, which leads to quite different asymptotic models for the shallow and deep cases, when $\alpha = O(\epsilon^2)$ and $\alpha = O(\epsilon)$, respectively. The typical representative of the first (shallow) case is the well-known Korteweg–de Vries (KdV) equation, while for the second (deep) case the so-called Benjamin–Ono (BO) or intermediate long wave (ILW) equations can be derived.

As usual in formal asymptotics, there is no way of assessing *a priori* whether the range of validity of these approximations is large enough to include realistic fixed values of the parameters. Koop & Butler (1981) were probably the first to attempt to check whether the weakly nonlinear theories were robust enough to capture practical experiments. Their conclusions, based on observations of solitary waves with two immiscible fluids in a wave tank, were that the KdV model would perform fairly well over a wide range of amplitudes for the shallow configuration. Better agreement with data could be achieved, however, by including higher-order terms from the asymptotic expansion as the amplitude parameter α increased. The weakly nonlinear theory would perform poorly for just about all their observations in the deep configuration. Segur & Hammack (1982) confirmed this using salt stratified water. Kao, Pan & Renouard (1985) repeated the experiments in the shallow configuration, again using salt to stratify water in two nearly homogeneous layers, and found the KdV theory in 'superb' agreement with their experimental observations. Even within the shallow configuration, however, it has been known at least since the 1980s (Miles 1981; Amick & Turner 1986; Funakoshi & Oikawa 1986) that, in analogy with the free-surface case, waves in the shallow configuration have a maximum theoretical amplitude, a selection criterion that is missed by the KdV theory. This provides perhaps the clearest evidence of how weakly nonlinear theories fail to apply to large-amplitude regimes, in general. (The particular case of critical depth ratio $h_1/h_2=(\rho_1/\rho_2)^{1/2}$ provides an exception. For densities and thicknesses close to this ratio, the so-called KdV-modified KdV (KdV-mKdV) equation can be derived, and for near critical layer thickness, experimental observations (Michallet & Barthélemy 1998) have shown that wave characteristics are reproduced by solutions to the KdV-mKdV model. Although it supports a maximum-amplitude wave solution, for the non-critical case, the KdV-mKdV model is not valid for other wave amplitudes.)

With this in mind, the present paper constitutes an attempt at examining these issues of model validity by direct comparisons of analytical and numerical results from classical and recently derived strongly nonlinear asymptotic theories by Choi & Camassa (1999) with numerical simulations of the Euler equations and experimental data presented in Michallet & Barthélemy (1998) and in Grue *et al.* (1999). Throughout our study, we use solitary waves as a testbed for the practical applicability of the various theories. Although a rather special class of solutions, these waves do embody the balance between nonlinearity Although and dispersion that is an essential feature of large-amplitude wave dynamics in nature, and often offer the additional advantage of closed-form solutions. Moreover, from an experimental viewpoint, these waves are ideally suitable for accurate measurements of their main defining features, such as amplitude, wavelength and speed.

The paper is organized as follows. We review the general theory for internal waves at the interface of two immiscible and inviscid fluids under gravity and sketch the derivation of models that take into account the possibility of large displacements of the interface from its equilibrium position. In particular, in § 2 we look at a numerical model to determine solutions of the coupled Euler equations, which apply to all physical set-ups in this class of problems. We stress here that simplifications of the original Euler system require additional assumptions, and these are possible with the two configurations of most practical interest, shallow and deep. Section 3 focuses on results and observations pertaining to the shallow configuration. In particular, we examine a sequence of tests for solitary-wave profiles, amplitude, effective wavelength wave and fluid velocities. Section 4 does the same within the deep configuration, whereas § 5 examines how the transition between shallow and deep theories occurs from the modelling viewpoint.

Throughout the paper, we consider exclusively two-dimensional (one horizontal and one vertical) situations. However, we stress that the strongly nonlinear models we consider can be readily written for fully three-dimensional set-ups (see, e.g. Choi & Camassa 1996).

2. Background on fundamental theory and models

2.1. *Theory: Euler equations*

For an inviscid and incompressible fluid of density ρ_i, the velocity components in Cartesian coordinates (u_i, w_i) and the pressure p_i satisfy the continuity equation and the Euler equations,

$$u_{i_x} + w_{i_z} = 0, \tag{2.1}$$

$$u_{i_t} + u_i u_{i_x} + w_i u_{i_z} = -p_{i_x}/\rho_i, \tag{2.2}$$

$$w_{i_t} + u_i w_{i_x} + w_i w_{i_z} = -p_{i_z}/\rho_i - g, \tag{2.3}$$

where g is the acceleration due to gravity and subscripts with respect to space and time represent partial differentiation. In a two-fluid system, $i = 1$ ($i = 2$) stands for the upper (lower) fluid (see figure 1) and $\rho_1 < \rho_2$ is assumed for a stable stratification.

The boundary conditions at the interface are the continuity of normal velocity and pressure:

$$\zeta_t + u_1\zeta_x = w_1, \quad \zeta_t + u_2\zeta_x = w_2, \quad p_1 = p_2 \qquad \text{at} \quad z = \zeta(x,t), \tag{2.4}$$

where ζ is a displacement of the interface. At the upper and lower rigid surfaces, the kinematic boundary conditions are given by

$$w_1(x, h_1, t) = 0\,, \qquad w_2(x, -h_2, t) = 0, \tag{2.5}$$

where h_1 (h_2) is the undisturbed thickness of the upper (lower) fluid layer.

2.2. *Full Euler equations algorithm*

In order to find stationary solutions of the full Euler equations (2.1)–(2.3), we apply the numerical method described in Grue *et al.* (1999). To make the paper as self-contained as possible, we briefly review the method here.

The wave is modelled in a frame of reference moving with its wave speed c. In this frame of reference the interface is stationary. The velocities (u_l, w_l) in each layer can be represented by analytic functions $q_l = u_l - \mathrm{i}w_l$, in the upper ($l = 1$) and lower ($l = 2$) layer relative to the moving frame of reference. Cauchy's integral theorem applies on each layer, and yields a system of integral equations,

$$PV\int_I \frac{q_l(z)+c}{z'-z}\,\mathrm{d}z - \int_I \frac{q_l{}^*(z)+c}{z'-z^*+(-1)^l 2\mathrm{i}h_l}\,\mathrm{d}z^* = \begin{cases} (-1)^l 2\pi\mathrm{i}(q_l(z')+c), & z' \in \Omega_l \\ (-1)^l \pi\mathrm{i}(q_l(z')+c), & z' \in I, \end{cases} \tag{2.6}$$

where I is the interface and Ω_l are the interior of the upper ($l = 1$) and lower ($l = 2$) layer, respectively. The integrals preceded by PV are principal value integrals, but only for $z' \in I$.

Previous examples of computationally determined very large internal travelling waves have been either broad (Turner & Vanden-Broeck 1988) or steep and even overhanging (Pullin & Grimshaw 1988). To allow for the latter type of solutions, the elevation of the interface is not represented as a function of the horizontal coordinate. The interface is instead parameterized and modelled by $z = \chi(\xi)$, where $\chi(\xi)$ is a complex function of the real parameter ξ which is either monotonically increasing or decreasing along the interface. The kinematic condition at the interface now reads

$$-u_1\mathrm{Im}\{\chi_\xi\} + w_1\mathrm{Re}\{\chi_\xi\} = -u_2\mathrm{Im}\{\chi_\xi\} + w_2\mathrm{Re}\{\chi_\xi\}, \tag{2.7}$$

where the subscript denotes differentiation with respect to ξ.

The algorithm for solving the coupled system (2.6) relies on a suitably discretized approximation to the integrals. Depending on the nature of the solution, we may choose different ways of distributing the computational points along the interface. By distributing these points evenly along the interface, e.g. by setting the distance between adjacent points equal, we can obtain good accuracy even for very steep and overhanging interfaces. A computationally less expensive choice is to distribute the points evenly in the horizontal direction, which is appropriate for broad interface profiles.

In addition to equations (2.6), the pressure derived from the complex velocities q_1 and q_2 must be continuous at the interface. As a last equation, any physical quantity describing the solitary wave must be set first as a parameter from the outset, e.g. the wave amplitude, the wave speed or the volume. The latter parameter is the most convenient when searching for very broad solutions, as these necessarily carry large volumes (Rusås & Grue 2002).

The form of the discretized equations can be found in Grue *et al.* (1999). An extension of the method to three-layer fluids is described in Rusås & Grue (2002) for solitary waves and in Rusås (2000) for periodic waves.

2.3. *Strongly nonlinear models*

From the assumption that the thickness of at least one fluid layer is much smaller than the characteristic wavelength, models can be derived from the fundamental Euler equations without additional assumptions on the amplitude of the wave motion. For simplicity, we impose the condition that the top fluid surface be confined by a rigid lid. A free surface can be included without any conceptual difficulty. However, scaling considerations and the experiments show that free-surface activity is quite small with respect to that of the interface, and hence we will neglect the upper free-surface displacement consistently with our level of approximation.

2.3.1. *The strongly nonlinear model for shallow configuration*

When the wavelength is long compared to the total fluid depth, an asymptotic expansion in the small parameter $\epsilon = \lambda/h_1$ can be carried out, resulting in a (local) set of equations that couple interface location to the depth-averaged velocities in the layers (Choi & Camassa 1999). This system in dimensional form for the four unknowns $(\zeta, \overline{u}_1, \overline{u}_2, P)$ is

$$\eta_{1_t} + (\eta_1 \overline{u}_1)_x = 0, \qquad \eta_1 = h_1 - \zeta, \tag{2.8}$$

$$\eta_{2_t} + (\eta_2 \overline{u}_2)_x = 0, \qquad \eta_2 = h_2 + \zeta, \tag{2.9}$$

$$\overline{u}_{1_t} + \overline{u}_1 \overline{u}_{1x} + g\zeta_x = -\frac{P_x}{\rho_1} + \frac{1}{\eta_1}\left(\tfrac{1}{3}{\eta_1}^3 G_1\right)_x, \tag{2.10}$$

$$\overline{u}_{2_t} + \overline{u}_2 \overline{u}_{2x} + g\zeta_x = -\frac{P_x}{\rho_2} + \frac{1}{\eta_2}\left(\tfrac{1}{3}{\eta_2}^3 G_2\right)_x, \tag{2.11}$$

with G_i, $i = 1, 2$, given by

$$\overline{u}_i(x, t) = \frac{1}{\eta_i}\int_{[\eta_i]} u_i(x, z, t)\,\mathrm{d}z, \qquad G_i(x, t) = \overline{u}_{i\,xt} + \overline{u}_i \overline{u}_{i\,xx} - (\overline{u}_{i\,x})^2 = -\frac{\left({D_i}^2\zeta\right)}{\eta_i}. \tag{2.12}$$

Here $D_i \equiv \partial_t + \overline{u}_i \partial_x$, and $\int_{[\eta_i]}$ denotes $\int_\zeta^{h_1}$ or $\int_{-h_2}^{\zeta}$ according to whether $i = 1$ or 2, respectively. The two kinematic equations, (2.8) and (2.9), are exact while the dynamic equations, (2.10) and (2.11), have an error of $O(\epsilon^4)$. These four equations can be reduced to just two for two unknowns, ζ and (say) $\overline{u}_1$, by eliminating $\overline{u}_2$ and P via the exact relation

$$\overline{u}_2 = -\frac{\eta_1}{\eta_2}\,\overline{u}_1;$$

however, the resulting expression is somewhat less compact than that of system (2.10) and (2.11).

System (2.10) and (2.11) can be viewed as the extension to multiple layers of the equations introduced by Green & Naghdi (1976) for one homogeneous fluid layer with a constant-pressure free surface, and hence the set of equations (2.9) and (2.11) is often referred to as the Green–Naghdi (GN) system in the literature. In fact, the same system for a single-fluid layer with one horizontal dimension was derived earlier by Su & Gardner (1969) following a long-wave asymptotic approach similar to ours, while the original GN system was the outcome of an *a priori* ansatz on the structure of the velocity field, which is only approximately satisfied. Solitary wave solutions of system (2.8)–(2.11) can be determined in closed form by the nonlinear ordinary differential equation for travelling waves, $\zeta(x-ct) \equiv \zeta(X)$ (Miyata 1985).

Depending on the parameters of the set-up, solitary waves can be either of elevation or depression, moving with speed c related to its (signed) amplitude a by

$$\frac{c^2}{{c_0}^2} = \frac{(h_1-a)(h_2+a)}{h_1h_2 - \left({c_0}^2/g\right)a}, \tag{2.13}$$

where c_0 is the linear long wave speed defined by

$${c_0}^2 = \frac{gh_1h_2(\rho_2-\rho_1)}{\rho_1h_2+\rho_2h_1}$$

The amplitude is limited by a maximum interface displacement given by, respectively,

$$a_m = \frac{h_1 - h_2\sqrt{\rho_1/\rho_2}}{1+\sqrt{\rho_1/\rho_2}}, \qquad {c_m}^2 = g(h_1+h_2)\frac{1-\sqrt{\rho_1/\rho_2}}{1+\sqrt{\rho_1/\rho_2}}. \tag{2.14}$$

This maximum amplitude wave is, in fact, a degenerate form of a solitary wave, which actually assumes the form of a front.

2.3.2. *Leading-order horizontal velocity shear dependence on* **z**

An approximate relation between layer-averaged velocities $\overline{u}_1$ and $\overline{u}_2$ and local velocities $u_1(x,z,t)$ and $u_2(x,z,t)$ can also be provided from the strongly nonlinear model for every height z in layers 1 and 2, respectively. These expressions for local velocities are useful for comparisons with the experimental results, which are obtained through particle imaging velocimetry (PIV) in the shallow-water configuration. We have

$$u_2(x,z,t) = \overline{u}_2(x,t) + \left(\frac{(\eta_2(x,t))^2}{6} - \frac{(z+h_2)^2}{2}\right)\partial_x^2\,\overline{u}_2(x,t), \tag{2.15}$$

with $-h_2 < z < \zeta$ for the lower fluid. This expression is approximate, with the correction being of order $O(\epsilon^4)$ in non-dimensional notation. For travelling-wave solutions of the strongly nonlinear system with speed c, the averaged velocity and layer thickness are related by the exact expression

$$\overline{u}_2(X) = c\left(1 - \frac{h_2}{\eta_2(X)}\right),$$

with $X = x - ct$, so that equation (2.15) becomes in this case

$$u_2(X,z) = c\left[1 - \frac{h_2}{\eta_2} + \left(\frac{{\eta_2}^2}{6} - \frac{(z+h_2)^2}{2}\right)\left(\frac{h_2\eta_2''}{{\eta_2}^2} - \frac{2h_2(\eta_2')^2}{{\eta_2}^3}\right)\right], \tag{2.16}$$

where $\eta_2' \equiv \eta_{2X}$ and $\eta_2'' \equiv \eta_{2XX}$. By using this expression, it follows, for example, that for a solitary wave of depression moving to the right ($c > 0$) the lower fluid velocity varies from, say, a minimum for waves of depression

$$u_2|_{z=\zeta} = c\left(1 - \frac{h_2}{\eta_2} - \tfrac{1}{3}h_2\eta_2''\right)$$

attained at the interface, to a maximum of

$$u_2|_{z=-h_2} = c\left(1 - \frac{h_2}{\eta_2} + \tfrac{1}{6}h_2\eta_2''\right)$$

near the location $X = X_m$ of maximum displacement of the wave, where $\eta_2'' \equiv \eta_{2XX} > 0$ and $\eta_2' \equiv \eta_{2X} = 0$. Notice that in approaching the maximum amplitude wave as $a \to a_m$, $\eta_2'' \to 0$ at the location of maximum displacement, since the solitary waves become progressively 'flatter' in this limit. Hence, the z-correction to the fluid velocity becomes more and more negligible as $a \to a_m$ and the velocity profile tends to become progressively 'straighter' to coincide with its layer-averaged expression at the maximum.

The expression analogous to (2.16) for the upper fluid layer is

$$u_1(X,z) = c\left[1 - \frac{h_1}{\eta_1} + \left(\frac{{\eta_1}^2}{6} - \frac{(h_1-z)^2}{2}\right)\left(\frac{h_1\eta_1''}{{\eta_1}^2} - \frac{2h_1(\eta_1')^2}{{\eta_1}^3}\right)\right], \tag{2.17}$$

with the velocity being largest at the interface near the maximum displacement location $X = X_m$,

$$u_1|_{z=\zeta} = c\left(1 - \frac{h_1}{\eta_1} - \tfrac{1}{3}h_1\eta_1''\right).$$

2.3.3. *The strongly nonlinear model for the deep configuration*

Our strongly nonlinear model in a two-layer system with the upper layer being thin and the lower layer being deep is (Choi & Camassa 1999)

$$\zeta_t - [(h_1 - \zeta)\bar{u}_1]_x = 0, \tag{2.18}$$

$$\begin{aligned} \bar{u}_{1t} + \bar{u}_1\bar{u}_{1x} + g\left(\frac{\rho_2}{\rho_1} - 1\right)\zeta_x &= \left(\frac{\rho_2}{\rho_1}\right)\mathscr{T}[\zeta_{tt}] \\ &= \mathscr{T}[(h_1-\zeta)\bar{u}_1]_{xt}, \end{aligned} \tag{2.19}$$

where the non-local operator $\mathscr{T}$ is defined as

$$\mathscr{T}[f] = \frac{1}{2h_2}\,⨍_{-\infty}^{\infty} f(x')\coth\left[\frac{\pi}{2h_2}(x'-x)\right]\mathrm{d}x'. \tag{2.20}$$

The first equation is exact and expresses the conservation of mass for the upper layer, while the second momentum equation for the upper layer has an error of $O(\epsilon^2)$. The interface is mainly excited by the fluid motion of the upper layer and the effect of the less active deep lower layer appears only as the dispersive term in the right-hand side of (2.19) through the continuity of pressure. When compared with the theory of shallow configuration, it can be seen that the leading-order dispersive effects from the upper layer appear at the next order $O(\epsilon^2)$. Since the upper layer is assumed to be dynamically important for the model given by (2.18)–(2.19), the model should not be used for the case of $\rho_1/\rho_2 \to 0$, for which the model simply yields the linear evolution of surface waves in a single layer of finite depth h_2.

In the limit of infinitely deep lower fluid ($h_2 \to \infty$), the operator $\mathscr{T}$ becomes the Hilbert transform. The case of the thin lower layer and deep upper layer is easily accommodated by relabelling of the dependent variables and appropriate sign changes of gravity and polarity. In order to find solitary-wave solutions for $\zeta(x-ct)\equiv\zeta(X)$, the system of equations (2.18)–(2.19) can be reduced to an integro-differential equation which can be solved iteratively by using Newton–Raphson iteration combined with a pseudo-spectral method based on the fast Fourier transform (FFT). The number of modes (N) is typically chosen as $N=2^7$ for the computations in this work.

3. Shallow configuration

Next, we concentrate on the shallow configuration. In order to minimize clutter in the various plots, we carry out separate comparisons of similar data from models and experiments. Thus, because the Euler system is expected to be the model closest to reality (if viscous effects can be assumed to be small), and the strongly nonlinear model derives directly from Euler's with the single assumption of long-wave dynamics, we compare results from the Euler and the strongly nonlinear systems first.

We then compare several results from the strongly nonlinear model directly with experimental data by Grue *et al.* (1999). These experiments were carried out with miscible fluids, fresh water and brine. In contrast with the experiments for the deep configuration, where stratification is achieved with immiscible fluids (cf. § 4), the density difference between the fluids is thus limited by salt saturation and hence it is relatively small for the shallow configuration, with the sharpness of the interface limited by diffusivity. On the other hand, by achieving stratification with salt concentration, un-modelled effects from surface tension and viscosity differences are avoided for shallow-configuration data. Moreover, as illustrated below, the shallow- and deep-configuration experiments differ in their relative scales, with the deep configuration tank being about a quarter of the length and more than an order of magnitude smaller in cross-section. All of these differences conspire to test further the robustness of the various theoretical models.

3.1. *Strongly nonlinear model vs. Euler*

Throughout the tests in this section we use the following parameters: $h_1=15\,\mathrm{cm}$, $h_2=62\,\mathrm{cm}$, $\rho_1=0.999\,\mathrm{g\,cm^{-3}}$ and $\rho_2=1.022\,\mathrm{g\,cm^{-3}}$, or, by defining $H=h_1+h_2$, equivalently $h_2/H=0.8$ ($h_1/h_2=15/62=0.24$), and $\rho_1/\rho_2=0.977$. These correspond to that of the miscible fluids in the experiments by Grue *et al.* (1999).

We begin with the most direct comparison, that of wave profiles from the numerical computation of Euler *vs.* the analytic expression from the strongly nonlinear model. As the amplitude is varied progressively from small values, where weakly nonlinear theories such as KdV can be expected to be valid, the model is tested more as the amplitude values approach the maximum for the given configuration. As can be seen from figure 2, solitary-wave solutions of the strongly nonlinear model are quite close to Euler's throughout the range of amplitudes shown. The solid curves are obtained via the numerical integration of the Euler system while the (long) dashed curves are provided by the analytical solution of the strongly nonlinear system. Not unexpectedly perhaps, the largest discrepancies occur for waves in the mid-amplitude range, here between $|a|/h_1\simeq0.3$ and $|a|/h_1\simeq0.7$, where the effective wavelength is shortest and so a long-wave theory such as the strongly nonlinear model can be expected to fare the worst.

Next, we look at the variation of effective wavelength λ_I/h_1 and wave velocity c/c_0 with amplitude a/h_1, where λ_I is the integral wavelength introduced by Koop &

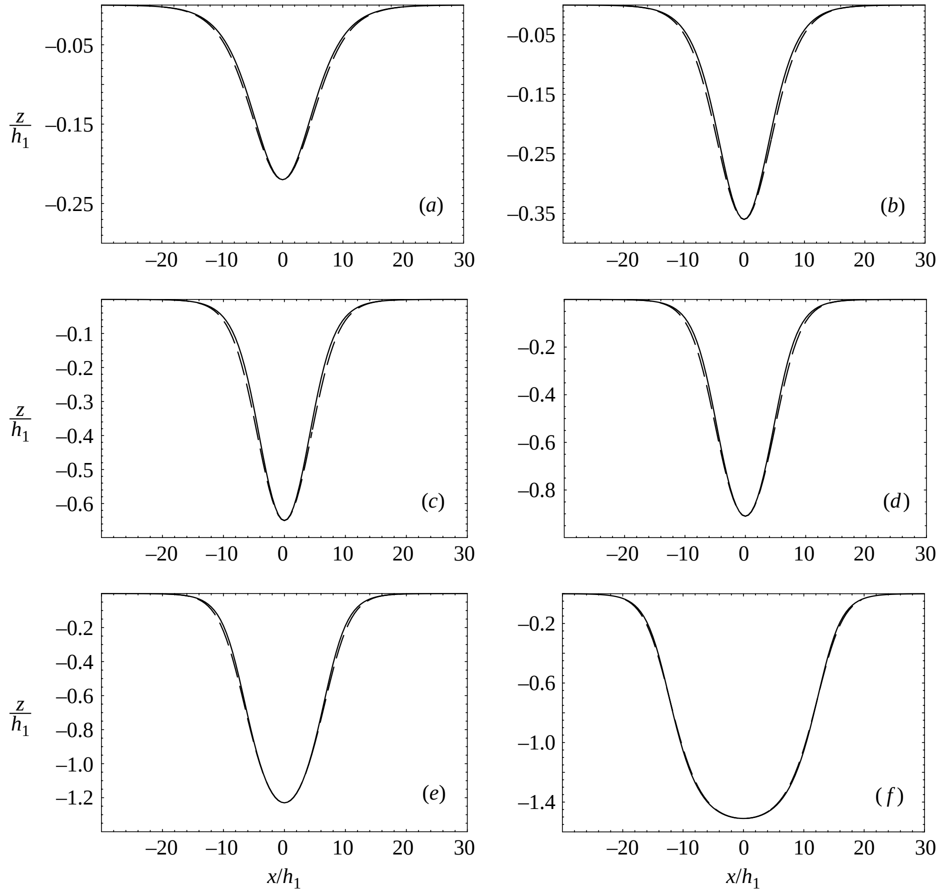

FIGURE 2. Solitary-wave profiles at increasing maximum displacement, for the case of miscible fluids with $\rho_1/\rho_2=0.999/1.022=0.977$, $h_2/H=0.8$ ($h_1/h_2=15/62=0.24$). Waves of depression are moving from left to right in this configuration and plot. Solid line: Euler computation. Dashed line: strongly nonlinear model solution. (*a*) $|a|/h_1=0.22$, (*b*) $|a|/h_1=0.36$, (*c*) $|a|/h_1=0.65$, (*d*) $|a|/h_1=0.91$ (*e*) $|a|/h_1=1.23$, (*f*) $|a|/h_1=1.51$. The maximum-amplitude wave for these parameters is $|a_m|/h_1=1.55$.

Butler (1981),

$$\lambda_I=\frac{1}{a}\int_{X_m}^{\infty}\zeta(X)\,\mathrm{d}X. \tag{3.1}$$

Once again, as demonstrated by figure 3, the agreement between Euler and the strongly nonlinear model is remarkable, with the largest discrepancy occurring in the mid-amplitude range. Notice that both wavelength and velocity plots terminate at the maximum amplitude a_m, whose value (2.14) is shared by both the Euler system and its strongly nonlinear model.

As our final comparison, we look at the variation of fluid velocity with depth. Expressions (2.16) and (2.17) allow reconstruction of the fluid velocity at height z from the knowledge of averaged velocity in each fluid layer. Figure 4 shows a comparison between the horizontal velocity profiles resulting from the numerical integration of the Euler equations and those from the strongly nonlinear theory (2.16) and (2.17) evaluated at $X=X_m$. Once again, the figure shows that, to the accuracy

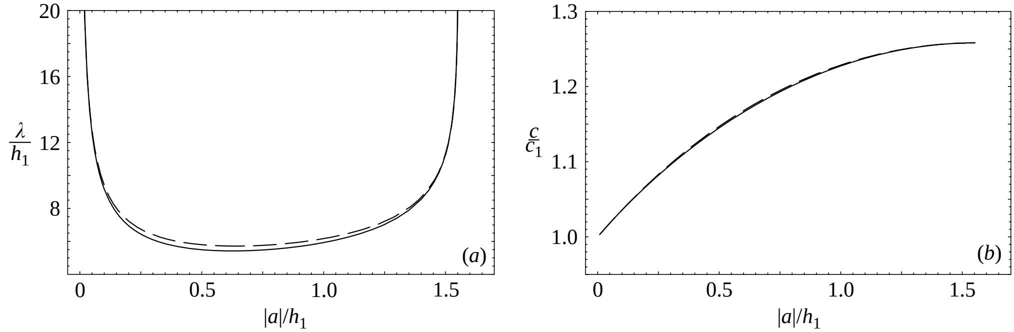

FIGURE 3. (*a*) Effective wavelength *vs.* amplitude. (*b*) Solitary wave speed *vs.* amplitude. Solid: Euler. Dashed: strongly nonlinear model. Parameters for this comparison: $h_1 = 15\,\text{cm}$, $h_2 = 62\,\text{cm}$, $\rho_1 = 0.999\,\text{g cm}^{-3}$ and $\rho_2 = 1.022\,\text{g cm}^{-3}$.

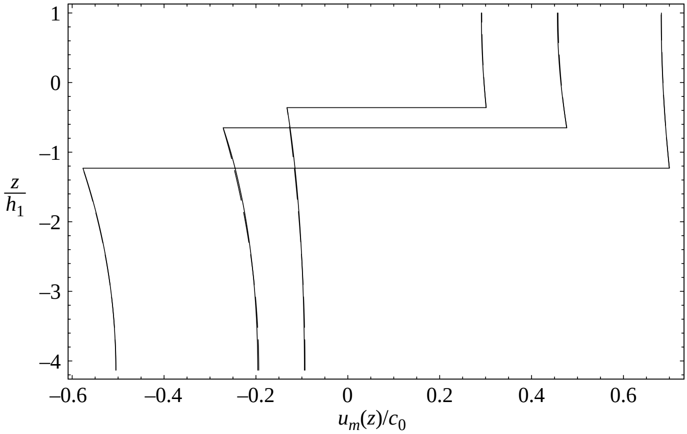

FIGURE 4. Velocity profiles $u_m(z)/c_0$ at the maximum interface displacement, for three solitary waves of amplitude $|a|/h_1 = 0.36$, $|a|/h_1 = 0.65$, and $|a|/h_1 = 1.23$, respectively, with miscible experiment parameters $\rho_1/\rho_2 = 0.999/1.022$, $h_2/H = 0.8$ ($h_1/h_2 = 15/62 = 0.24$). The horizontal lines are located at the maximum interface displacement, and profiles above (below) correspond to horizontal fluid velocity $u_1(X_m, z)$ ($u_2(X_m, z)$) of the upper (lower) fluid. The solid curves are produced by numerical integration of the Euler equations, the dashed curves (barely discernible being so close to the Euler theory) are the strongly nonlinear expressions (2.16) and (2.17).

of the graphics, the Euler solutions and the strongly nonlinear model are equivalent. Again, the trend for better agreement as the largest-amplitude wave is approached can be noticed in the figure.

3.2. *Strongly nonlinear model vs. experiments*

We now focus on testing the performance of the strongly nonlinear model with respect to experimental data pertaining to the shallow-water configuration. All of the data reported in this section had been collected in the experimental investigations by Grue *et al.* (1999), and Sveen *et al.* (2002), although some of the data have been re-processed here for the present comparison. Notice that the wave profiles are reconstructed by converting the time record of interface displacement at fixed location along the wave tank into spatial coordinates via the measured wave speed, $x = ct$.

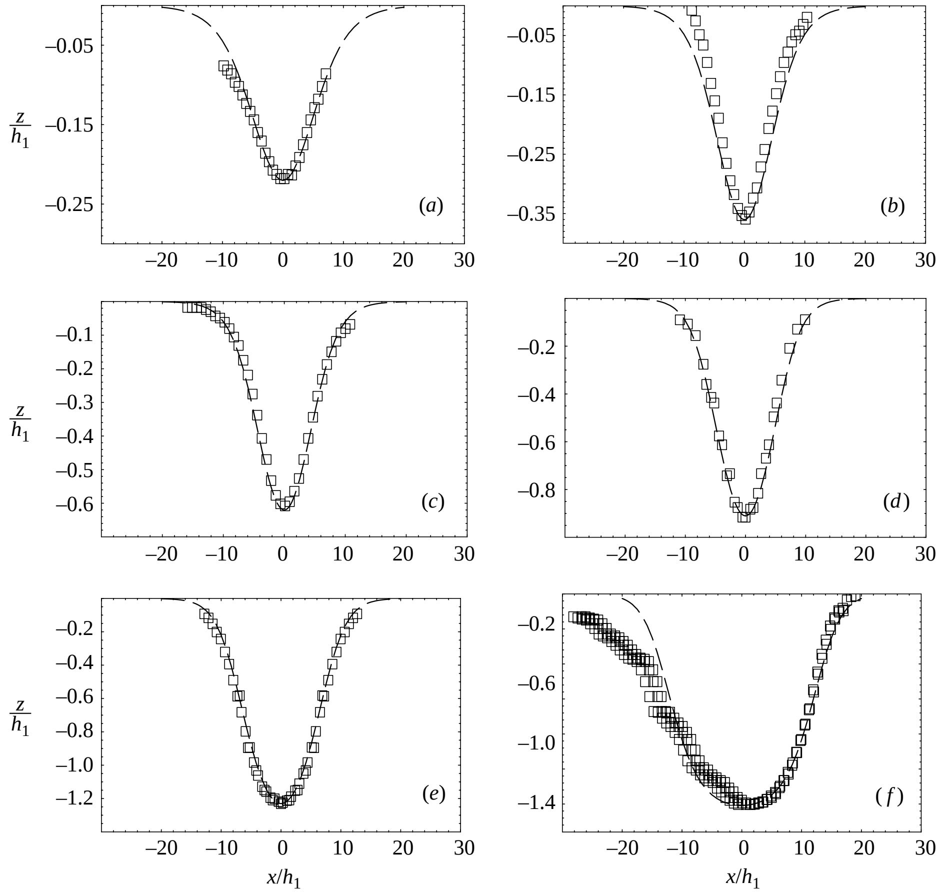

FIGURE 5. Similar to figure 2, but with experimental data collected by Grue *et al.* (1999), instead of Euler computations. Miscible fluid case, with $\rho_1/\rho_2 = 0.999/1.022 = 0.977$, $h_2/H = 0.8$ ($h_1/h_2 = 15/62 = 0.24$). Measured interface displacement from experiment (symbols) and strongly nonlinear model solution (dashes lines), for (*a*) $|a|/h_1 = 0.22$, (*b*) $|a|/h_1 = 0.36$, (*c*) $|a|/h_1 = 0.62$, (*d*) $|a|/h_1 = 0.91$ (*e*) $|a|/h_1 = 1.23$, (*f*) $|a|/h_1 = 1.51$. Notice the data in the back of the wave in (*f*), indicating instability setting in near the maximum displacement of interface for waves close to the maximum amplitude $|a|/h_1 = 1.55$.

Figure 5 presents experimental data for wave profiles together with those from the strongly nonlinear theory. The wave profiles are computed from the solution of the travelling-wave equation at several different amplitudes using the measured parameters of the experiment. These amplitudes and parameters correspond to those used in figure 2 for the Euler and strongly nonlinear model wave profiles, and comparing with this figure it can be seen that, from the viewpoint of these experimental data, the Euler and strongly nonlinear model solutions are indistinguishable.

The data in figure 5(*f*) show the effects of breaking in the back of the wave, whose measured amplitude ($|a|/h_1 = 1.51$) is close to the maximum amplitude ($|a_m|/h_1 = 1.55$) for this set-up. As can be expected from instabilities of shear flows, the breaking occurs near the wave crest, where the velocity jump across the interface is the largest. The instabilities then destroy the smoothness of the interface in the wave's wake. Notice, however, that the front of the wave remains smooth and in good agreement with the theory.

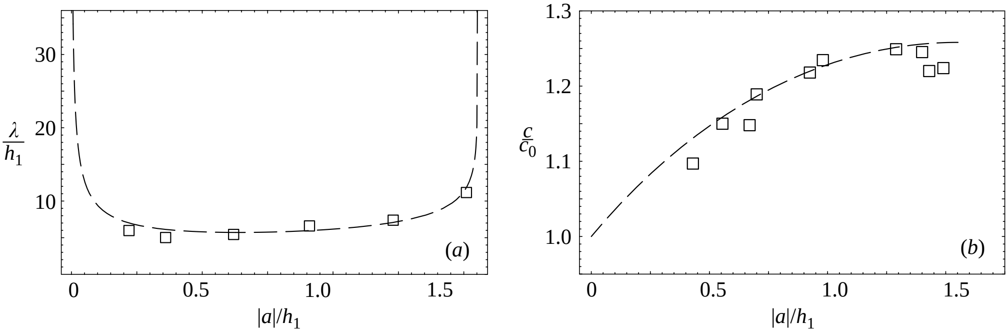

FIGURE 6. Strongly nonlinear model *vs*. experimental data: speed and effective wavelength as in figure 3. Miscible fluid case, with $\rho_1/\rho_2 = 0.999/1.022 = 0.977$, $h_2/H = 0.8$ ($h_1/h_2 = 15/62$). Experimental data (symbols) collected by Grue *et al.* (1999), and strongly nonlinear model solution (dashed lines).

Next, the experimental data for variation of effective wavelength and wave speed with amplitude are compared with the corresponding strongly nonlinear model curves. Measurements of effective wavelength are performed using the measured waveforms shown in figure 5. We note that because the recording techniques applied, the interface measurements are truncated at the wings of the waves. This is because several video cameras were used to record images to one video recorder, one at a time. Because of this truncation, the measured effective wavelengths should be expected to be smaller than the theoretically predicted wavelengths. The difference between the experimentally obtained and the theoretically predicted wavelengths varies from about 24 % in figure 5(*a*) to about 4 % in figure 5(*f*). As we can see in figure 6, the agreement between the data and the model is reasonable. Discrepancies seem to occur mostly at the lower and largest amplitudes. Although we do not have a clear explanation for this discrepancy, it seems natural to think that wave breaking near the maximum amplitude should play a role in affecting the wave speed, whereas viscosity could be playing a more prominent role for low amplitudes, thereby making any Euler-based model less accurate.

Figure 7 provides a comparison between the wave-induced horizontal velocity shear profiles computed from the model (2.16) and (2.17) and the data collected via PIV measurements. The agreement is again satisfactory, even for a wave displacement as large as $|a|/h_1 = 1.23$. Small discrepancies are not easily attributed to any specific effect, although a departure from the idealization of two layers can be expected to play a role. Certainly, the good agreement between Euler's and the model's results displayed in figure 4 points to effects other than the approximations used in the derivation of the model from the parent Euler system.

4. Deep configuration

In this section, we consider internal waves for the deep configuration, for which the thickness of one fluid layer is much larger than that of the other, while being comparable to or greater than the characteristic wavelength. We first compare numerical solutions of the model (2.18)–(2.19) with those obtained from the Euler equations. We then compare experimental results by Michallet & Barthélemy (1998) with those from the strongly nonlinear model. The wave flume used in these experiments is approximately 3 m long and has a 15 cm × 10 cm cross-section. Thus,

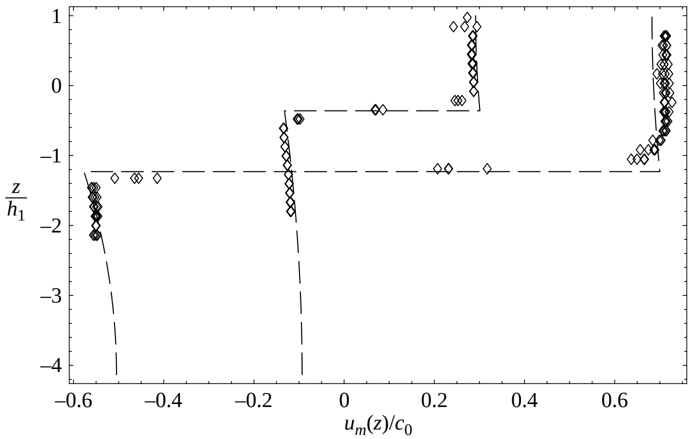

FIGURE 7. Analogue of figure 4, model *vs.* experiment: velocity profiles $u_m(z)/c_0$ at the maximum interface displacement, for two solitary waves of amplitude $|a|/h_1 = 0.36$, and $|a|/h_1 = 1.23$, respectively, *vs.* PIV measurements with the shallow configuration miscible set-up, $\rho_1/\rho_2 = 0.999/1.022$, $h_2/H = 0.8$ ($h_1/h_2 = 15/62 = 0.24$). The horizontal lines are located at the maximum interface displacement, and profiles above (below) correspond to horizontal fluid velocity $u_1(X_m, z)$ ($u_2(X_m, z)$) of the upper (lower) fluid. The dashed curves are the strongly nonlinear expressions (2.16) and (2.17), the symbols are the horizontal velocity measurements from the experiment by Grue *et al.* (1999).

the scale of the deep-configuration experiment is much smaller than that of the shallow regime, where the channel had dimensions 12.3 m with cross-section 0.5 m × 1 m. The two fluids chosen are immiscible liquids having different specific gravities, respectively, petrol product 'Exxsol D60' (density $\rho_0 = 0.78\,\mathrm{kg\,l^{-1}}$, viscosity $\nu = 1.64\,\mathrm{m^2\,s^{-1}}$) and water ($\rho = 1\,\mathrm{kg\,l^{-1}}$). Immiscible fluid systems are convenient to use: no mixing occurs at the interface, which is thus always well defined. On the other hand, unlike the case of brine and fresh water, physical properties other than density variations, such as viscosity mismatch and surface tension, may play a role. Also, we remark that fluid velocity measurements are much more delicate in this situation than in the shallow-onfiguration case above. This is due in part to the difficulty of seeding both fluids with particles that are locally neutrally buoyant. This is one of the reason why PIV data are not reported for the experiments in the deep-configuration case.

4.1. *Strongly nonlinear model vs. Euler*

For the comparison between model and Euler solutions, we choose two depth ratios, $h_1/h_2 = 1/24$, or equivalently $h_2/H = 0.96$ and $h_1/h_2 = 1/99$ (or $h_2/H = 0.99$). The first ratio is the one actually achieved in the experimental results which we use later. The extent to which the lower layer can be considered deep in these two cases depends on the typical wavelength and is not clear *a priori*; the comparison will provide an indication of which regime can be considered as falling within the asymptotic theory for the strongly nonlinear model.

As shown in figure 8, the deep analogue of figure 2 for the shallow configuration, the solitary-wave solutions of the model are very close to the Euler solutions for small values of wave amplitude, but, as the wave amplitude increases, the comparison becomes quickly less favourable. A similar observation can also be made for the wave speed and the effective wavelength from figure 9. Notice that the effective wavelength of the Euler solutions increases with wave amplitude much more rapidly than that of our solutions of the asymptotic model. This shows that, for this depth ratio, the

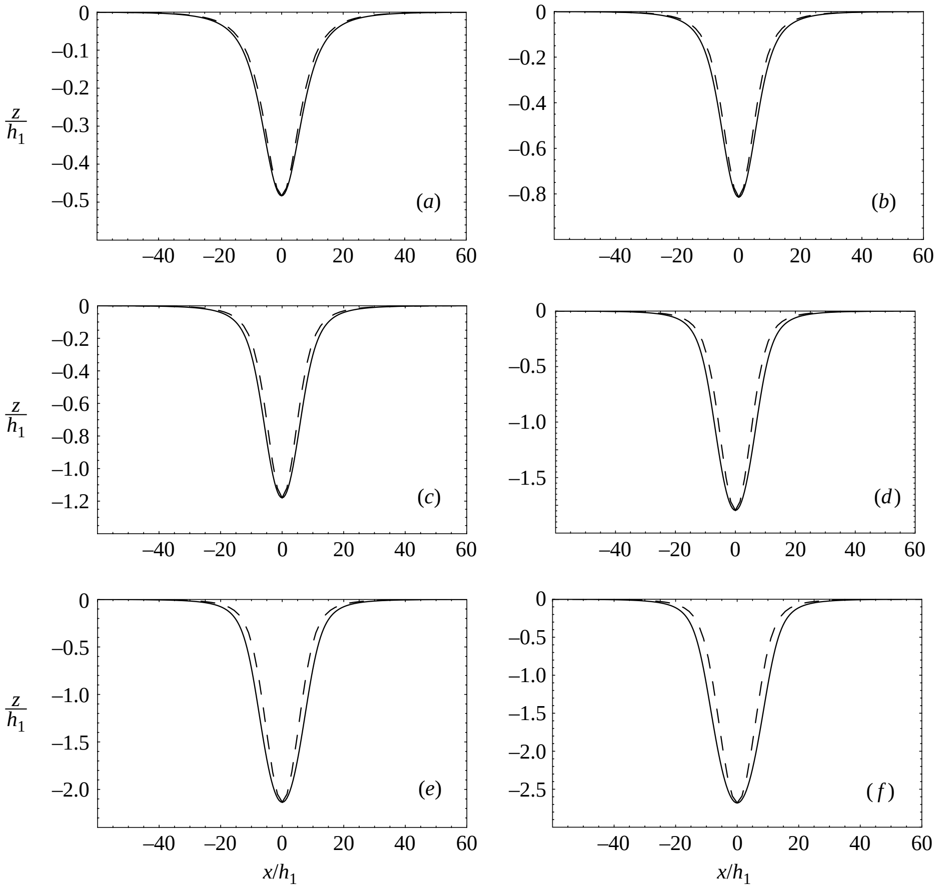

FIGURE 8. Solitary-wave profiles at increasing maximum displacement, for the case of immiscible fluids with $\rho_1/\rho_2 = 0.78$, $h_2/H = 0.96$ ($h_1/h_2 = 0.54/12.94 \simeq 1/24$). Solid line: Euler computation. Dashed line: strongly nonlinear model. (*a*) $|a|/h_1 = 0.4834$, (*b*) $|a|/h_1 = 0.8143$, (*c*) $|a|/h_1 = 1.1797$, (*d*) $|a|/h_1 = 1.7955$, (*e*) $|a|/h_1 = 2.1353$, (*f*) $|a|/h_1 = 2.681$.

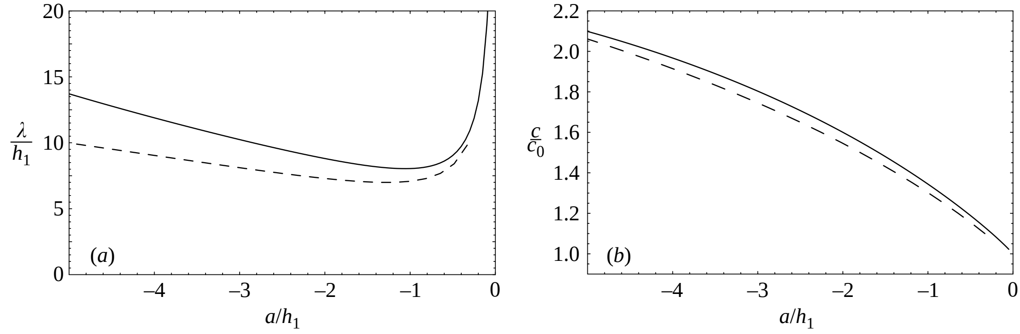

FIGURE 9. (*a*) Effective wavelength *vs.* amplitude. (*b*) Solitary wave speed *vs.* amplitude. Solid: Euler. Dashed: strongly nonlinear model (2.18)–(2.19). Parameters of the immiscible fluid experiments: $\rho_1/\rho_2 = 0.78$, $h_2/H = 0.96$ ($h_1/h_2 = 0.54/12.94 \simeq 1/24$).

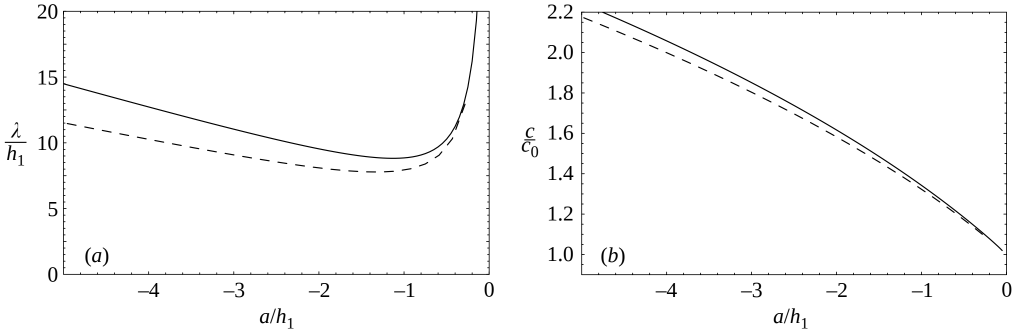

FIGURE 10. Same as figure 9 but for 'deeper' aspect ratio $h_2/H = 0.99$ ($h_1/h_2 = 1/99$).

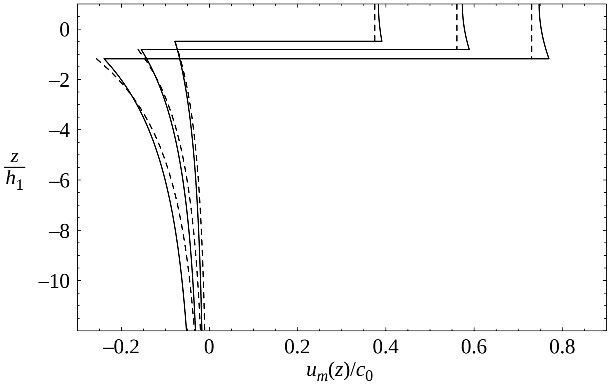

FIGURE 11. Velocity profiles $u_m(z)/c_0$ at the maximum interface displacement for the deep configuration of $h_2/H = 0.96$ with immiscible fluids $\rho_1/\rho_2 = 0.78$. The horizontal lines are located at the maximum interface displacement, and profiles above (below) correspond to horizontal fluid velocity $u_1(X_m, z)$ ($u_2(X_m, z)$) of the upper (lower) fluid. The solid curves are produced by numerical integration of the Euler equations, while the dashed curves are $u_1(X_m, z) = \overline{u}_1(X_m)$ for the upper layer and $u_2(X_m, z) = \phi_{2X}(X_m, z)$ for the lower layer, where ϕ_2 is the velocity potential satisfying the Laplace equation with $\phi_{2_z}(X, z) = -c\zeta_X(X)$. Velocity profiles for three solitary waves of amplitude $|a|/h_1 = 0.48$, $|a|/h_1 = 0.81$, and $|a|/h_1 = 1.17$, respectively.

effective wavelength is larger than the thickness of the (deep) lower layer for large-amplitude solitary waves, so that these waves are too wide for the deep-configuration asymptotic assumptions to be valid.

In figure 11, we consider the variation of fluid velocity with depth. Notice that the derivation of the model for the deep configuration uses the leading-order approximation to the velocity field, by which the depth variation of velocity for the shallow upper layer is neglected, while the linear theory is used for the deep lower-layer. As the wave amplitude increases, we can expect that the nonlinear dispersive effects of the thin upper layer become more important, thereby making comparison with the Euler solutions worse. On the other hand, incorporating these additional dispersive effects, while straightforward for the upper layer, increases substantially the complexity of the lower-layer model, and, as we shall see, it is not clear to what extent the extra complexity justifies the increase in the range of validity of the model.

Figures 10 and 12, where the depth of the lower layer has been increased to a depth ratio of $h_2/H = 0.99$, show that, even for this slight increase of depth ratio with respect to that of $h_2/H = 0.96$, the agreement between solutions of the Euler

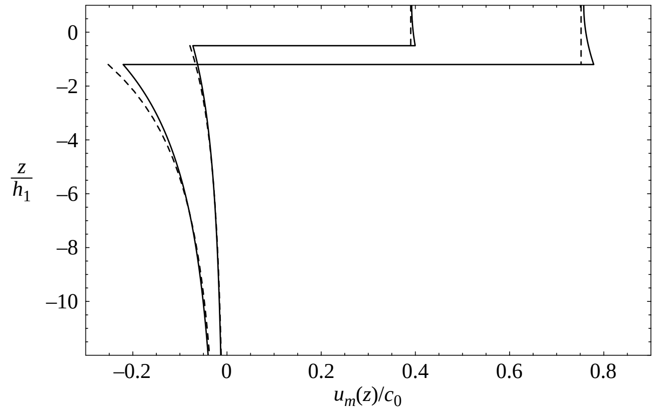

FIGURE 12. Same as previous figure, but with $h_2/H = 0.99$. Velocity profiles for two solitary waves of amplitude $|a|/h_1 = 0.5$ and $|a|/h_1 = 1.2$, respectively.

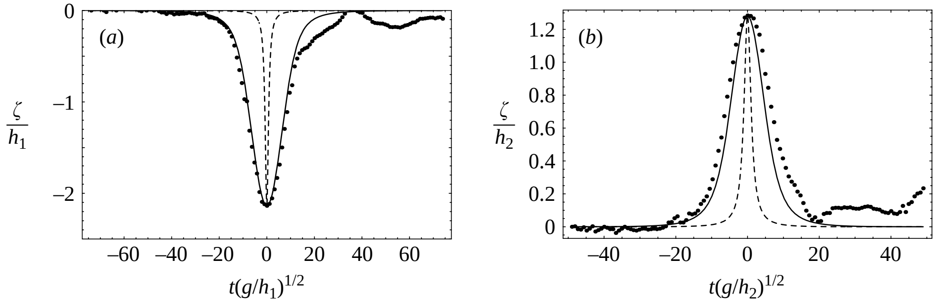

FIGURE 13. Wave profiles for deep configuration with $\rho_1/\rho_2 = 0.78$: experimental data (dots) collected in Michallet & Barthélemy (1998), strongly nonlinear theory (solid line), weakly nonlinear ILW theory (dashed line). (*a*) $h_2/H = 0.96$ ($h_1/h_2 = 0.54/12.94 = 1/24$), (*b*) $h_2/H = 0.09$ ($h_1/h_2 = 9.32/0.92 = 10.13$).

equations and those of the asymptotic model improves noticeably. Thus, we can conclude that the validity of the model for the deep configuration is somewhat limited to intermediate wave amplitudes and the model for the deep configuration should be used with caution (as expected) as soon as the transition between deep and shallow configurations, as measured by closeness to the maximum-amplitude wave for a given depth, is approached with increasing amplitudes. However, it must be remarked that stability issues might dominate the dynamics of large-amplitudes waves, so that this intermediate regime could very well cover most of what is observable in practice.

4.2. *Strongly nonlinear model vs. experiments*

For the comparison of numerical solutions of the asymptotic model with experimental data, we chose two different depth ratios, $h_2/H = 0.96$ ($h_1/h_2 = 1/24$) and $h_2/H = 0.09$ ($h_1/h_2 = 10.13$). The first depth ratio is for the case of the thin upper and deep lower layers for which the governing equations are given by (2.18)–(2.19), while the second is for the opposite case of a thicker upper layer. As shown in figure 13, the numerical solitary-wave solutions of the model show good agreement with the experimental data (except at the trailing tails in the experiments). The fact that the model predicts slightly narrower wave profiles than the experiments is consistent with the observation made in the comparison between the Euler equations and the model. We can see from these

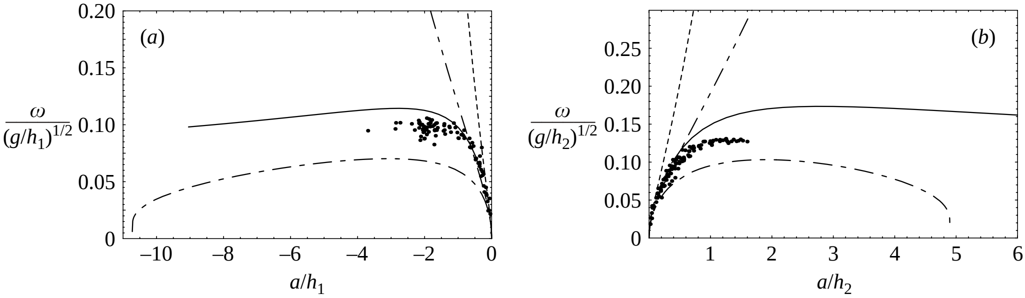

FIGURE 14. Effect wavelength (wave frequency) *vs.* amplitude for deep-configuration with $\rho_1/\rho_2 = 0.78$: experimental data (dots) collected in Michallet & Barthélemy (1998), deep-configuration theory (solid line), weakly nonlinear ILW theory (— — —), strongly nonlinear shallow-configuration theory (—-—), weakly nonlinear shallow-configuration KdV theory (—--—). (*a*) $h_2/H = 0.96$ $(h_1/h_2 = 0.54/12.94 = 1/24)$, (*b*) $h_2/H = 0.09$ $(h_1/h_2 = 9.32/0.92 = 10.13)$.

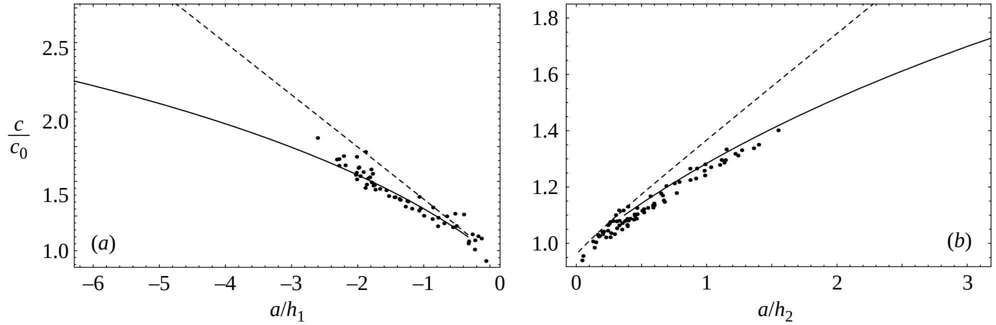

FIGURE 15. Wave speed *vs.* amplitude for the deep configuration: experimental data (dots) collected in Michallet & Barthélemy (1998), strongly nonlinear theory (solid line), weakly nonlinear ILW theory (dashed line). (*a*) $h_2/H = 0.96$ $(h_1/h_2 = 0.54/12.94 = 1/24)$, (*b*) $h_2/H = 0.09$ $(h_1/h_2 = 9.32/0.92 = 10.13)$.

comparisons that weakly nonlinear theories are completely ineffective for describing solitary waves of these wave amplitudes, and the higher-order nonlinearity in the asymptotic model is essential in describing nonlinear internal waves.

We also compare the model's solutions with experimental data of the characteristic wave frequency and wave speed for varying wave amplitude. The wave frequency is defined (Michallet & Barthélemy 1998) as

$$\omega = 2a \bigg/ \int_{-\infty}^{\infty} \zeta(x,t)\,\mathrm{d}t. \tag{4.1}$$

As shown in figure 14, although the asymptotic theory slightly overestimates the wave frequency over the range of wave amplitudes considered, it improves the match with experimental data with respect to the weakly nonlinear theory (ILW). Notice that the strongly nonlinear theory for the shallow configuration is not applicable to these depth ratios, but the experimental data show a tendency to approach the shallow-configuration theory for larger values of wave amplitude. The wave speed for the deep-configuration model increases at a slower rate than that of the weakly nonlinear model, as can be seen in figure 15, and shows good agreement with the experimental data.

5. The transition from shallow to deep configuration

The strongly nonlinear asymptotic models for the Euler equations that we have introduced and tested rely on the assumption of either shallow or deep fluid layers. In order to explore the domain of validity of these models, we examine how their solitary-wave solutions behave with respect to depth ratio by comparison with numerical solutions of the full Euler system.

In principle, by progressively increasing one of the two fluid layers, we would expect the contrast between solitary-wave solutions of the Euler system and those of the strongly nonlinear model for the shallow configuration to increase, while the agreement with corresponding solutions of the deep configuration model ought to improve. However, notice that for any finite fluid layers, there still exists a wave of maximum amplitude. In fact, while it is doubtful (but not strictly proved) that the deep-configuration strongly nonlinear model supports a maximum-amplitude wave, both the strongly nonlinear model and Euler systems have limiting wave solutions of similar front-like form occurring at exactly the same amplitude. Being a front, the effective wavelength tends to infinity as the maximum amplitude is approached, so that the wave can again be viewed as long with respect to both fluid depths. In this limit, it can be expected that the solutions of the shallow-configuration model recover good agreement with the Euler ones. Of course, a large depth ratio increases the size of the velocity jump at the interface, and so waves approaching the maximum amplitude would presumably be unobservable when one fluid layer is much larger than the other, owing to the shear instabilities that would develop in this case. For a fixed (large) depth ratio, we therefore expect that the deep-configuration model works only for a finite range of wave amplitudes, while the domain of validity for the deep configuration model becomes wider as the depth ratio increases.

We compare the Euler solution with those from the shallow- and deep-configuration models in figure 16, which shows the (right-half) wave profiles as the amplitude increases for three depth ratios: $h_2/H = 0.9$, $h_2/H = 0.96$ and $h_2/H = 0.99$. We present only the data for the lowest-amplitude wave from the strongly nonlinear deep model (2.18)–(2.19) (dot-dash curves) for each case of depth ratio, as this model cannot work well for higher amplitudes, as mentioned before. For a fixed depth ratio, the theory for the deep configuration yields a better agreement with the Euler equations than the shallow-configuration model when waves are small (but still quite large compared with the undisturbed upper-layer thickness as in case (*b*) and (*c*) of the figure, where the amplitude is more than twice and ten times h_1, respectively). The opposite is true for large-amplitude waves. Notice that the major deviations of theory of the shallow configuration from the Euler computation for these large depth ratios occur in the wave's wings, which are noticeably smaller for the Euler wave profiles. This can also be seen by the plots of effective wavelength *vs.* amplitude depicted in figure 17. By observing the Euler curves in figure, it is tempting to conjecture that the $\lambda(a)$ relations parameterized by h_2/H admit an envelope that in the limit $h_2/H \to 1$ approaches a straight line (of slope $\simeq 2$ for this particular density ratio). In contrast, the curves in figure 17 suggest that their envelope for solitary waves of the strongly nonlinear model is far from linear, and as $h_2/H \to 1$, the shallow-configuration waves carry a much larger volume than their Euler counterparts.

Next, in order to further test the performance of the models with respect to the Euler system, we compare effective wavelength and wave speed *vs.* increasing depth ratio h_2/H (the counterpart of figure 17), for solitary waves at fixed amplitudes that can be considered large with respect to the upper-layer undisturbed thickness h_1. Of course, solitary waves of a certain amplitude a can be supported only for depth

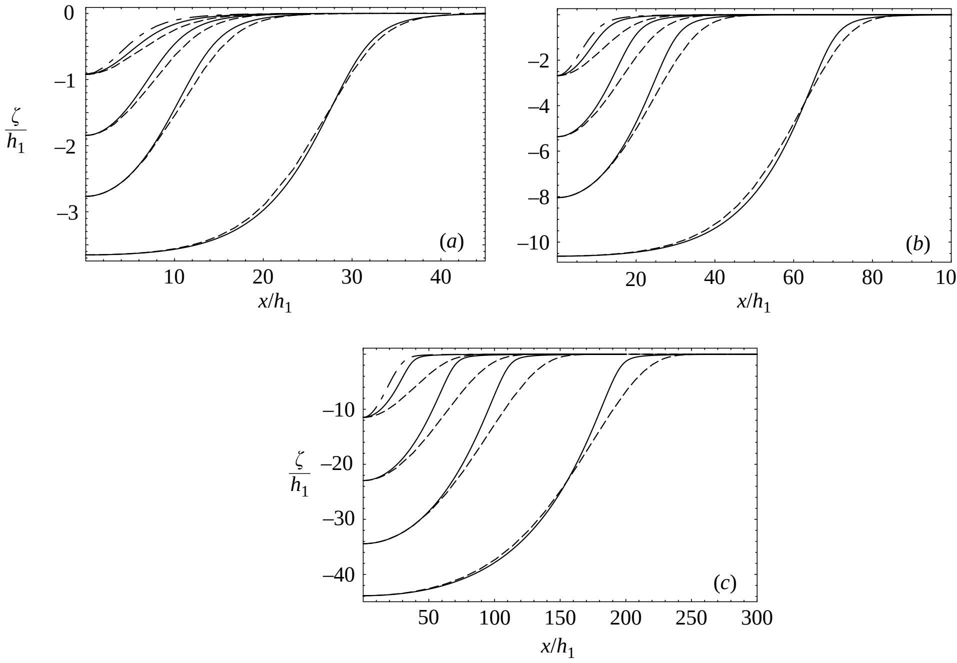

FIGURE 16. Plot of wave profiles at scaled amplitudes a varying in increments of 25 % of limiting amplitude a_m, with the largest waves being $0.99\,a_m$. The density ratio is that of the immiscible fluid experiments, $\rho_1/\rho_2 = 0.78$. Solid curve: Euler. Dashed curve: strongly nonlinear model for shallow configuration (2.8)–(2.11). Dot-dashed: deep configuration model in (2.18)–(2.19). (*a*) $h_2/H = 0.9$ $(h_1/h_2 = 1/9)$, (*b*) $h_2/H = 0.96$ $(h_1/h_2 = 1/24)$, (*c*) $h_2/H = 0.99$ $(h_1/h_2 = 1/99)$. Largest wave in case (*c*) is $0.937\,a_m$. In order to emphasize the differences among the models, only half of the wave profile to the right of the maximum displacement of the interface is shown here.

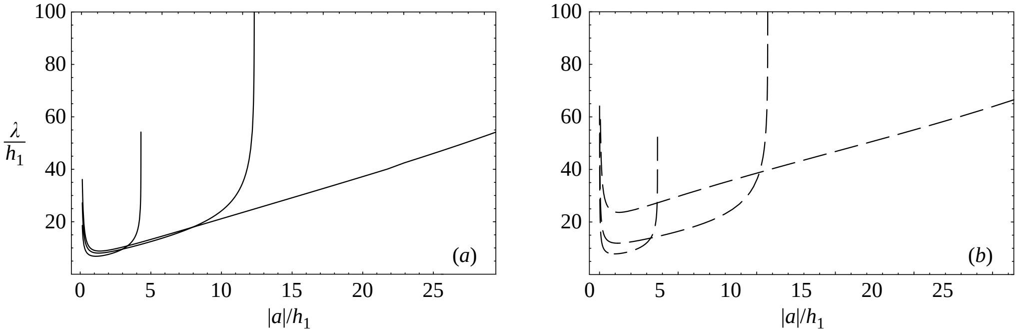

FIGURE 17. Effective wavelength *vs.* amplitude curves for increasing values of the depth ratio parameter h_2/H. (*a*) Euler computation. (*b*) Strongly nonlinear model for shallow configuration (2.8)–(2.11). Density ratio of the immiscible fluid experiments, $\rho_1/\rho_2 = 0.78$. Three curves are plotted for $h_2/H = 0.9$, 0.96, 0.99, respectively, corresponding to increasing values of the maximum amplitude $|a_m|$ (identical for both Euler and strongly nonlinear model) at which the effective wavelength becomes infinite. Notice the rapid increase of $|a_m|$ for the transition from $h_2/H = 0.96$ to 0.99: the vertical asymptote at $|a_m|/h_1 = 45.9$ for $h_2/H = 0.99$ is omitted to retain some detail in the horizontal range of amplitudes for the smaller depth ratios.

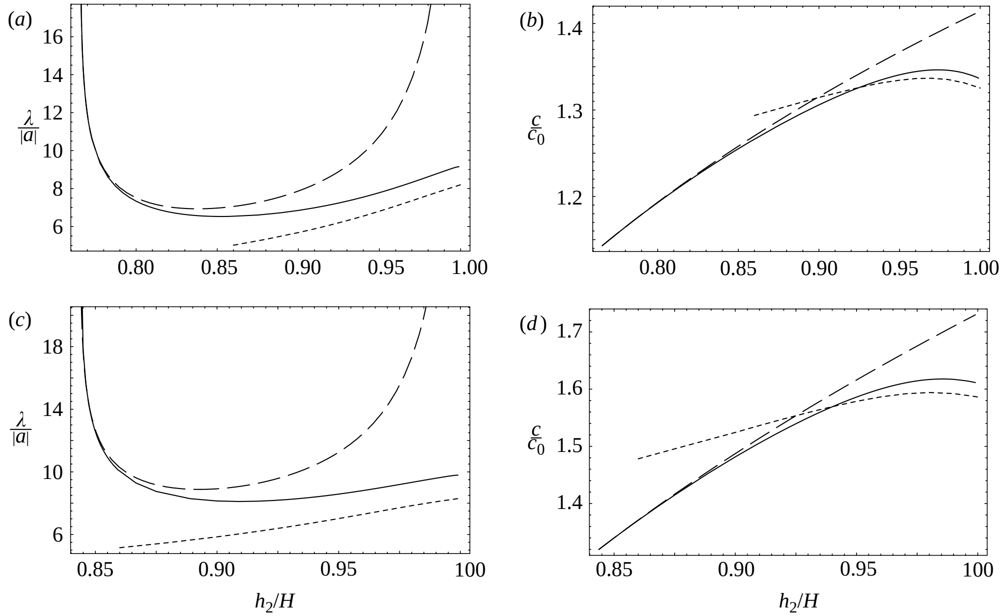

FIGURE 18. Curves of effective wavelength, (*a*) and (*c*), and velocity, (*b*) and (*d*), *vs.* depth ratio parameter h_2/H at fixed-amplitude values. Solid curve: Euler computation; long-dash: strongly nonlinear model for shallow configuration (2.8)–(2.11); short-dash: strongly nonlinear model for deep configuration (2.18)–(2.19). Density ratio of the immiscible fluid experiments, $\rho_1/\rho_2 = 0.78$. Cases (*a*) and (*b*) correspond to fixed amplitude $a/h_1 = -1$, while for cases (*c*) and (*d*) the amplitude is fixed to $a/h_1 = -2$. Waves of fixed amplitude exist only for thickness ratios larger than a minimum value fixed by the amplitude (cf. (2.14)); the maximum thickness ratio for all cases here is $h_2/H = 0.999$.

ratios larger than the value at which $a = a_m$, according to (2.14). Figure 18 shows the result for the two amplitudes $a/h_1 = -1$ and $a/h_2 = -2$, with the density ratio of the immiscible fluid experiment $\rho_1/\rho_2 = 0.78$. For these two amplitudes, it is evident that the shallow-water configuration becomes inadequate at relatively large aspect ratios $h_2/H \simeq 0.9$, while the deep configuration model does well in qualitative predictions such as slope and convexity with increasing aspect ratios past $h_2/H > 0.98$, but suffers somewhat in quantitative agreement, especially for the effective wavelength. It should be noted, however, that these amplitudes correspond to rather strong nonlinear waves, probably near the limits of what can be observed in experiments and in the field, and the agreement improves with lower amplitudes, as the comparison between the $a/h_1 = -2$ and the $a/h_1 = -1$ cases show.

6. Discussion

We have presented a comparison between experimental, analytical and numerical results for internal waves in two-layer fluids, devoted to assess the applicability and test the limitations of various levels of mathematical theories available for such systems. Experimental results refer to both miscible and immiscible fluids, where large-amplitude travelling waves comparable to the thickness of at least one of the layers are generated in set-ups that strive to minimize effects assumed to be small in the theory. The analytical results are obtained mainly from asymptotic models, which have been appropriately generalized so that they can support the highly nonlinear regimes observed experimentally. The Euler equations arguably offer the most comprehensive level of description of our physical set-ups, provided viscous (and diffusive, for miscible fluids) effects can be considered negligible. However, extracting information from the Euler system almost invariably requires numerical assistance, which can become quite intensive when moving two-dimensional wave patterns and long time scales are considered.

Several conclusions can be drawn from our investigation. First, as usual with asymptotic theories which rely on small parameters, it is hard to determine *a priori* how small is 'small'. One way to assess this is by direct comparison with solutions of the parent equation, and, in turn, with dedicated experimental results, as we have now done. From this, we can see that the strongly nonlinear model for the shallow configuration is fairly robust, in the sense that it does not require an overly small long-wave parameter for a favourable comparison with the Euler theory, and it performs well even for fairly skewed depth ratios, at least as far as our solitary wave test is concerned. This remains true across all types of comparison that we have used, from the basic waveform test to the horizontal fluid parcel velocity profiles *vs.* depth. Moreover, for the shallow configuration, our measurements show that both the asymptotic model and the fundamental Euler theory are within experimental accuracy.

In contrast to this robustness, the strongly nonlinear model for the deep configuration is more fragile and must be used with some caution. With an aspect ratio in which the thin layer is only a few per cent of the total depth, it is still possible to detect finite-depth effects when comparing to the Euler results for the type of waves we have considered. So, for instance, as the sequence of figures 8–10 shows, simply moving from an aspect ratio $h_2/H = 0.96$ (the one which is experimentally available) to the slightly larger ratio of $h_2/H = 0.99$ substantially improves the comparison between the strongly nonlinear model and the Euler computations. Similarly, the transition study of § 5 shows that a depth ratio $h_2/H = 0.9$ is certainly not sufficient to bring forth deep-configuration effects, and while no longer viable for depth ratios $h_2/H \geqslant 0.96$, the strongly nonlinear theory for shallow configuration does manage to capture the bulk features of large-amplitude waves when compared to the Euler computations.

All of our tests focused on solitary waves. By combining the nonlinearity and dispersion of water-wave dynamics, this is an interesting class of solutions, and one that arises in a variety of physical situations; however, it remains to be seen how successfully the various models are in rendering (some of) the truly time-dependent interface dynamics available to two- or multiple-fluid-layer systems, especially when the homogeneous-layer assumption is only approximately satisfied. A comparison with unsteady Euler solutions will be a first step in further establishing the validity of the asymptotic models. By restricting to two spatial dimensions, Euler computations can be carried out numerically for sufficiently long times and with sufficient accuracy. In this respect, we remark here that both the strongly nonlinear model and the Euler theory are affected by Kelvin–Helmholtz instability, owing to the velocity jump at the interface (see figures 4, 11, and 12) and some form of regularization is necessary to implement consistent numerical algorithms (Liska, Margolin & Wendroff 1995; Jo & Choi 2002). For the case of immiscible fluids, such regularization is naturally provided by surface tension, at least for the Euler theory, but for miscible fluids, regularizing effects come from more complicated interfacial physics, such as diffused interfaces and viscosity. Further modelling at both the Euler and asymptotic level are necessary to isolate the regularizing physical mechanisms in this case, such as the inclusion of a thin third layer with continuous density transition.

Finally, we stress that the strongly nonlinear models for both configurations are not limited to one horizontal dimension, as in the present study, and these models can easily be written (Choi & Camassa 1996) for two horizontal dimensions. Moreover, extension of the present two-layer case to that of multiple layers is straightforward (Choi 2000), as is the inclusion of bottom topographic forcing, provided it varies gently enough so as to be compatible with the long-wavelength assumption. In fact, we think that the main advantage afforded by the models lies in the two-(horizontal) dimensional setting, whereby all dynamic terms are explicitly included, as opposed to the limitations imposed by the implicit constraint on the velocity owing to the pressure/Poisson-equation component in Euler computations. As is well known, this aspect of the Euler system can make highly nonlinear realistic regimes very expensive in a direct numerical approach.

R. C. gratefully acknowledges support from NSF through Grant DMS-0104329, and NATO-CRG 950897. W. C. also acknowledges the support from the Rackaham Graduate School of the University of Michigan. H. M. gratefully acknowledges the financial support of CNRS and the continuous friendly scientific support by Professor Eric Barthélemy. J. K. S. gratefully acknowledges the support by Professor John Grue, Dr Atle Jensen, Mr Arve Kvalheim and Mr Svein Vesterby. J. K. S.'s research was performed under the Strategic University Programme 'General Analysis of Realistic Ocean Waves', funded by the Norwegian Research Council. R. C. and W. C. were supported in part by the DOE CCPP and BES programs during some of the early stages of this work. We thank an anonymous referee for suggesting the title of our paper.

REFERENCES

Amick, C. J. & Turner, R. E. L. 1986 A global theory of internal solitary waves in two fluid systems. *Trans. Am. Math. Soc.* **298**, 431–484.

Baines, P. G. 1995 *Topographic Effects in Stratified Shear Flows.* Cambridge University Press.

Choi, W. 2000 Strongly nonlinear internal waves in a multilayer system. *Fifth Intl Symp. on Stratified Flows* (ed. by G. Lawrence, R. Pieters & N. Yonemitsu), vol. 2 737–742.

Choi, W. & Camassa, R. 1996 Weakly nonlinear internal waves in a two-fluid system. *J. Fluid Mech.* **313**, 83–103.

Choi, W. & Camassa, R. 1999 Fully nonlinear internal waves in a two-fluid system, *J. Fluid Mech.* **396**, 1–36.

Funakoshi, M. & Oikawa, M. 1986 Long internal waves of large amplitude in a two-layer fluid. *J. Phys. Soc. Japan* **55**, 128–144.

Green, A. E. & Naghdi, P. M. 1976 A derivation of equations for wave propagation in water of variable depth. *J. Fluid Mech.* **78**, 237–246.

Grue, J., Jensen, A., Rusas, P. E., & Sveen, J. K. 1999 Properties of large-amplitude internal waves. *J. Fluid Mech.* **380**, 257–278.

Jackson, C. R. 2004 An atlas of internal solitary-like waves and their properties. http://www.internalwaveatlas.com/Atlas2_index.html.

Jo, T. & Choi, W. 2002 Dynamics of strongly nonlinear solitary waves in shallow water. *Stud. Appl. Maths* **109**, 205–228.

Kao, T. W., Pan F.-S. & Renouard, D. 1985 Internal solitons on the pycnocline: generation, propagation, and shoaling and breaking over a slope. *J. Fluid Mech.* **159**, 19–53.

Koop, C. G. & Butler, G. 1981 An investigation of internal solitary waves in a two-fluid system. *J. Fluid Mech.* **112**, 225–251.

Liska, R., Margolin, L. & Wendroff, B. 1995 Nonhydrostatic two-layer models of incompressible flow. *Computers Math. Applic.* **29**, 25–37.

LIU, A. K., CHANG, Y. S., HSU, M.-K. & LIANG, N. K. 1998 Evolution of nonlinear internal waves in the East and South China Seas. *J. Geophys. Res.* **103**, 7995–8008.

MICHALLET, H. & BARTHÉLEMY, E. 1998 Experimental study of interfacial solitary waves. *J. Fluid Mech.* **366**, 159–177.

MILES, J. W. 1981 On internal solitary waves II. *Tellus* **33**, 397–401.

MIYATA, M. 1985 An internal solitary wave of large amplitude. *La mer* **23**, 43–48.

ORR, M. H. & MIGNEREY, P. C. 2003 Nonlinear internal waves in the South China Sea: observation of the conversion of the depression internal waves. *J. Geophys. Res. Oceans* **108**, 3064.

PEDLOSKY, J. 1979 *Geophysical Fluid Dynamics*. Spinger.

PULLIN, D. J. & GRIMSHAW, R. H. J. 1988 Finite-amplitude solitary waves at the interface between 2 homogeneous fluids. *Phys. Fluids* **31**, 3550–3559.

RUSÅS, P. O. 2000 On nonlinear internal waves in two- and three-layer fluids. DSc thesis, Department of Mathematics, University of Oslo.

RUSÅS, P. O. & GRUE, J. 2002 Solitary waves and conjugate flows in a three-layer fluid. *Eur. J. Mech.* B/*Fluids* **21**, 185–206.

SEGUR, H. & HAMMACK, J. L. 1982 Soliton models of long internal waves. *J. Fluid Mech.* **118**, 285–304.

STANTON, T. P. & OSTROVSKY, L. A. 1998 Observation of highly nonlinear internal solitons over the continental shelf. *Geophys. Res. Lett.* **25**, 2695–2698.

SU, C. H. & GARDNER, C. S. 1969 Korteweg–de Vries equation and generalization III: derivation of the Korteweg–de Vries equation and Burgers equation. *J. Math. Phys.* **10**, 536–539.

SVEEN, J. K. & COWEN, E. A. 2004 Quantitative imaging techniques and their application to wavy flow. In *PIV and Water Waves* (ed. J. Grue, P. L. F. Liu & G. K. Pedersen) World Scientific, Singapore.

SVEEN, J. K., GUO, Y., DAVIES, P. A. & GRUE, J. 2002 On the breaking of internal solitary waves at a ridge. *J. Fluid Mech.* **469**, 161–188.

TURNER, R. E. L. & VANDEN-BROECK, J. M. 1988 Broadening of interfacial solitary waves. *Phys. Fluids* **31**, 2486–2490.

ZENG, K. & ALPERS, W. 2004 Generation of internal solitary waves in the Sulu Sea and their refraction by bottom topography studied by ERS SAR imagery and a numerical model. *Intl J. Remote Sensing* **25**, 1277–1281.